Low-Temperature-Graphitized and Interpenetrating Network C/Fe₃O₄ Magnetic Nanocomposites with Enhanced Tribological Properties under High Temperature

Yuying Chen, Qing Yang, Wenqin Lu, Yanjuan Zhang, Zuqiang Huang, Huayu Hu,* and Tao Gan*

Cite This: *ACS Appl. Mater. Interfaces* 2022, 14, 33922−33932

Read Online

ACCESS | Metrics & More | Article Recommendations | SI Supporting Information

ABSTRACT: Although the core−shell structure magnetic nanocomposites have been widely used as lubricant additives, their tribological properties are still poor under high temperature and high load. Herein, the graphitized C/Fe₃O₄ magnetic nanocomposites (g-C/Fe₃O₄) with an interpenetrating network structure were successfully fabricated by an in situ hydrothermal carbonization method combined with a subsequent ball milling process at room temperature. The results showed that the ball milling process not only promoted the transformation of graphitized carbon but also effectively eliminated the interfacial effect between carbon and Fe₃O₄. Moreover, the g-C/Fe₃O₄ used as a lubricant additive in rapeseed oil exhibited excellent tribological properties and high thermo-stability under 155 °C and 980 N, with the friction coefficient reduced by 32.8% compared to the independent Fe₃O₄. The enhanced tribological performance of g-C/Fe₃O₄ could be attributed to the graphitized carbon and its interpenetrating network structure under low load force (392 N), while under high load force (980 N), it could be ascribed to the synergistic effect between the graphitized carbon and magnetic Fe₃O₄ nanoparticles. This work not only offers a method for the synthesis of nanocomposite lubricant additives but also shows great potential in practical applications for high-temperature tribology.

KEYWORDS: *interpenetrating network structure, C/Fe₃O₄ nanocomposites, low-temperature graphitization, tribological properties, high-temperature tribology*
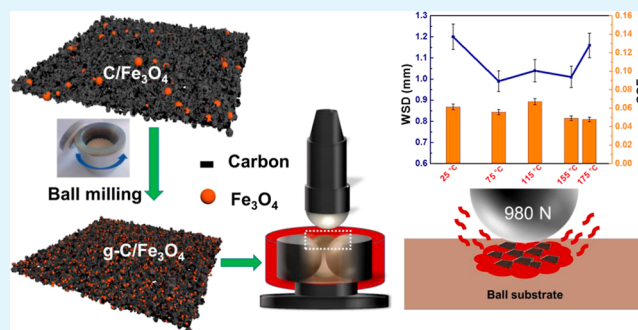
1. INTRODUCTION

Friction can be seen everywhere in our daily life, reducing friction and wear can effectively extend the service life of a machine, reduce energy consumption, and have a huge role in promoting industrial development. Recently, nanomaterials including metal nanoparticles (NPs), inorganic NPs, and polymer NPs have been used as lubricant additives, which show outstanding anti-friction and anti-wear properties.[1−3] Among them, magnetic NPs, such as MnZnFe₂O₄, CoFe₂O₄, and Fe₃O₄, have received widespread attention because of their potential to reduce the cost of treatment and recycle waste oil.[4−6] These magnetic nanomaterials are easily adhered on the surface of the friction pair due to their magnetism. Therefore, a friction self-healing film is formed on the sliding surface, which has an anti-friction effect. Especially, due to their non-toxic nature, environmental friendliness, and low cost, Fe₃O₄ NPs are commonly used in the application of lubricant additives.[7] For instance, Song et al.[8] have synthesized the magnetite submicrometer Fe₃O₄ spheres by pulsed laser ablation synthesis crystallization technology, which showed a good lubrication effect. Previous studies have found that Fe₃O₄ NPs can induce chemical reactions under the effect of friction, thus forming a

layer or layers of self-healing protection films rich in Fe, FeO, Fe₃O₄, γ-FeOOH, α-Fe₂O₃, and γ-Fe₂O₃ on the friction contact surface.[9,10] However, due to their high surface energy and strong magnetic properties, the dispersion stability of Fe₃O₄ NPs is poor in the process of friction, which will contact grinding grain, resulting in severe wear.

Currently, in order to solve the problems of easy aggregation and poor dispersion of Fe₃O₄ NPs, core−shell structure magnetic composites, such as Fe₃O₄@C, Fe₃O₄@GO, and Fe₃O₄@MoS₂, have been studied as lubricant additives.[11−15] Huang, et al.[16] prepared magnetic core−shell Fe₃O₄@C microspheres by a two-step synthesis method, compared with the independent Fe₃O₄, the friction coefficient and wear scar width of Fe₃O₄@C in sunflower oil decreased by 18.9 and 25.9%
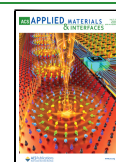
under 5 N, respectively, which indicated a synergistic effect between the carbon layer and magnetic Fe_3O_4 NPs. Meanwhile, the carbon layer can effectively improve the dispersion performance of Fe_3O_4 NPs to prevent agglomeration in the process of friction. However, the effect of the amorphous carbon film on improving friction is limited, and it mainly plays the role of load bearing, while graphene additives can effectively improve the lubricant effect by forming a thick friction film.[17] For instance, Sammaiah et al.[18] synthesized the GO-Fe_3O_4 nanohybrids by a co-precipitation method, which exhibited better anti-friction and anti-wear properties than those of Fe_3O_4-based ferrofluids. Compared with $Fe_3O_4@C$, the two-dimensional lamellar structure of GO is easier to enter the friction interface, resulting in better friction reduction. Meanwhile, the polar oxygenated functional groups of GO make the binding sites for Fe_3O_4 NPs form GO-based nanohybrids, which are more stable than $Fe_3O_4@C$ microspheres. Although the composites with core−shell structures show superior anti-friction performance under low load force, Fe_3O_4 and carbon in those composites will be peeled off at high load, thus showing poor tribological performance.

In space environments, under the condition of poor heat dissipation, the huge friction heat is difficult to dissipate in time, resulting in an increase in the temperature of lubricating oils, and that high temperature will affect the service life of the protective oxide film formed by lubricant additives on contact surfaces during the rubbing process. Thus, it is urgent to prepare a high-temperature lubricant additive for practical engineering applications. Recently, graphitized carbon composites, such as g-C_3N_4, graphene, and phosphorus-graphene (P-Gr) hybrids, used as lubricant additives have achieved satisfactory tribological performances under high temperature and high load.[19−21] For example, Wu et al.[21] developed a phosphorus-graphene (P-Gr) hybrid by high-energy ball-milling, which exhibited an excellent tribological performance at 100 N and 100 °C, including a low friction coefficient of 0.112 (12% reduction) and good anti-abrasion. The carbon atoms on the surface of graphitized carbon are sp^2 hybridized and have a hexagonal graphite crystal structure. The advantage of the hexagonal graphite crystal structure is that it is easily converted into larger and more ordered graphene at a high temperature, which makes it easier to form a physical protective film under high load, thereby achieving superior low friction.[22] Moreover, the negatively charged graphitic carbon is easily and quickly adsorbed on the positively charged metal surface, and the graphitic carbon acts as a bearing ball in the initial stage, producing a rolling effect on the contact surface, which can minimize the sliding friction and thus reduce the friction coefficient. Currently, several synthetic methods for graphitizing carbon materials, such as high-temperature heat treatment, a catalyst, electrochemical, and ball milling, have been studied.[23−26] Therein, the ball milling method has the advantages of being low-cost, eco-friendly, and easy-to-operate, which shows great potential in practical application.[27] Zhang and Li[28] prepared the carbonaceous intermediates as lubricant additives in a high-energy ball mill, which showed that the ball milling process leads to a decrease in the graphite micro-crystalline size and an increase in interlayer spacing. Furthermore, interpenetrating network structural composites have been widely used in various fields such as coatings, sealants, adhesives, and so on because of their barrier-free penetration diffusion and outstanding thermal stability.[29−31] Therefore, to make full use of the advantages of

graphitized carbon and magnetic Fe_3O_4, we designed a magnetic nanocomposite with an interpenetrating network structure to resolve the problems of core−shell materials; meanwhile, the nanocomposites are graphitized by the ball milling process for the improvement of the anti-friction and anti-wear properties at high temperatures.

In this study, the graphitized C/Fe_3O_4 magnetic nanocomposites (g-C/Fe_3O_4) with interpenetrating network structures were successfully fabricated by the in situ hydrothermal carbonization method combined with the subsequent ball milling process at room temperature. Specifically, using pretreated cassava starch as a carbon source and $FeCl_3$ as an iron source, the pretreated starch and $FeCl_3$ were added into a hydrothermal reactor for hydrothermal carbonization to obtain C/Fe_3O_4, then, the mixture of C/Fe_3O_4 and polyvinylpyrrolidone (PVP) water solution was ball milled in a planetary ball mill to obtain g-C/Fe_3O_4. The tribological properties of g-C/Fe_3O_4, C/Fe_3O_4, Fe_3O_4, and hydrothermal carbon used as lubricant additives in rapeseed oil were comparatively discussed on the four-ball friction and a wear tester, and their extreme pressure effects were also investigated. In addition, the friction and wear mechanisms were examined by employing X-ray photoelectron spectra (XPS) and Raman spectra. This study aims to pave the way for the preparation of high-temperature lubricant additives to fulfill the practical engineering application requirements.

2. EXPERIMENTAL SECTION

2.1. Materials. $FeCl_3$ (≥ 99.9%, Shanghai Aladdin Biochemical Technology Co., Ltd), cassava starch (Guangxi Nongken Mingyang Biochemical Group Co., Ltd), ethylene glycol (EG, ≥ 99.9%, Guangdong Guanghua Sci-Tech Co., Ltd), ammonia solution (25−28%, Guangdong Guanghua Sci-Tech Co., Ltd), PVP (Sigma-Aldrich, China), and anhydrous ethanol were used as received. All chemicals used throughout this study were of analytical grade, and they were used without further purification.

2.2. Preparation of C/Fe_3O_4 Nanocomposites. The pretreatment of cassava starch was performed in a customized stirring ball mill.[32,33] 400 mL zirconium balls, 40.0 g of dried cassava starch, and 1.0 g of $FeCl_3$ were added to the jacketed stainless-steel ball-milling tank, and the outer layer of the ball-milling tank was added with constant temperature circulating water at 50 °C and then reacted at 300 rpm for 1 h. Finally, pretreated starch was obtained by screening. Subsequently, C/Fe_3O_4 nanocomposites were prepared by an in situ hydrothermal method. In a typical synthesis process, 4.0 g of pretreated starch was dissolved in 80 mL of deionized water. Then, a certain amount of $FeCl_3$ and EG added to the above solution with stirring at 60 °C. Finally, the solution was transferred to a 100 mL autoclave, and 0.8 mL of $NH_3·H_2O$ was added and then heated at 160 °C for 11 h under nitrogen protection and at 300 rpm speed. After the reaction, the samples were separated by magnetic separation and washed with ethanol and deionized water several times. Freeze-dried black and magnetic powder was obtained, which was denoted as C/Fe_3O_4. The preparation method of hydrothermal carbon and Fe_3O_4 NPs was similar to that of C/Fe_3O_4, except no $FeCl_3$ or pretreated starch was added, respectively.

2.3. Preparation of Graphitized C/Fe_3O_4 Nanocomposites. The graphitization of C/Fe_3O_4 nanocomposites was carried out in a planetary ball mill. 1.0 g of C/Fe_3O_4 particles, 50 mL of as-prepared PVP water solution (8 mg/mL), and zirconium balls ($d = 1$ mm) according to the ball material ratio of 50:1 were added into the ball mill tank and then ground for 5 h at 500 rpm. After ball milling, deionized water and ethanol were washed many times to remove PVP, dried in a DZF-6020 vacuum drying oven, and denoted as g-C/Fe_3O_4.

2.4. Characterization. The crystal phase structure information of the sample was obtained by X-ray diffraction (XRD) measurements using the Rigaku D/Max 2500V X-ray diffractometer ($\lambda = -K\alpha$). The

Figure 1. Synthesis schematic of the g-C/Fe$_3$O$_4$ nanocomposites.
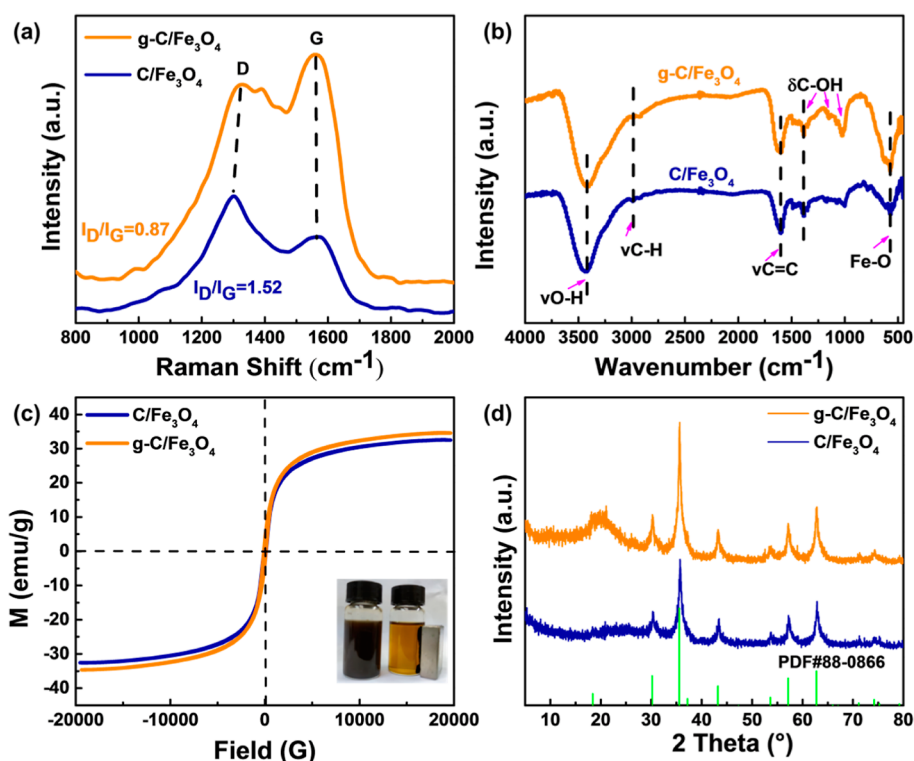
Figure 2. (a) Raman spectra, (b) FT-IR spectra, (c) VSM curves, and (d) XRD patterns of g-C/Fe$_3$O$_4$ and C/Fe$_3$O$_4$ nanocomposites.

detailed morphology and microstructure of C/Fe$_3$O$_4$ nanocomposites before and after ball milling were investigated by scanning electron microscopy (SEM + EDS, Hitachi S-4800, Japan) and transmission electron microscopy (TEM + EDS, FEI Tecnal G2 F20, USA). The functional groups of C/Fe$_3$O$_4$ nanocomposites before and after ball milling were obtained by Fourier transform infrared spectroscopy (FT-IR, Nicolet iS 50, USA). A vibrating sample magnetometer (VSM, Lakeshore 7410, USA) was a measurement technique for determining the magnetism of C/Fe$_3$O$_4$ and g-C/Fe$_3$O$_4$ nanocomposites. Raman spectroscopy (Horiba Scientific LabRAM HR Evolution) characterized the degree of graphitization of the samples. X-ray photoelectron spectroscopy (XPS, Thermo Scientific K-Alpha, USA) was performed to probe the chemical state of the samples. Nanoparticle size analyzers (Nano-ZS90X, UK) characterized the particle size of nanocomposites. An elemental analyzer (Elementar: Vario EL cube, DE) and an inductively coupled plasma emission spectrometer (ICP-OES, Agilent 720ES(OES), USA) were used to analyze the elemental content of the nanocomposites. 3D contour of

the worn zones was measured employing Keyence VHX-7000 at 392 N load. SEM micrographs of the surfaces of preweld balls + energy-dispersive X-ray spectroscopy (EDS) were also investigated. The elemental state of the worn zone lubricant was analyzed by XPS.

2.5. Tribological Properties. C/Fe$_3$O$_4$ and g-C/Fe$_3$O$_4$ nanocomposites were added into rapeseed oil to form several diverse concentration solutions by ultrasonication. Then, the MRS-10A microcomputer-controlled four-ball friction and wear-testing machine (Jinan YiHua Tribology Testing Technology Co. Ltd., China) were used to test the extreme pressure performance at room temperature and tribological performance at a high temperature, respectively. The extreme pressure performance of lubricating oil was expressed by the maximum card bit load (P_B). The greater the P_B value, the better the extreme pressure performance. The friction and wear of additives in lubricating oil at different temperatures, concentrations, and loads were investigated. All the long grinding experiments were carried out at 1200 rpm for 30 min. The test method of the extreme pressure was carried out according to the GB/T 3142-82 method for testing. The
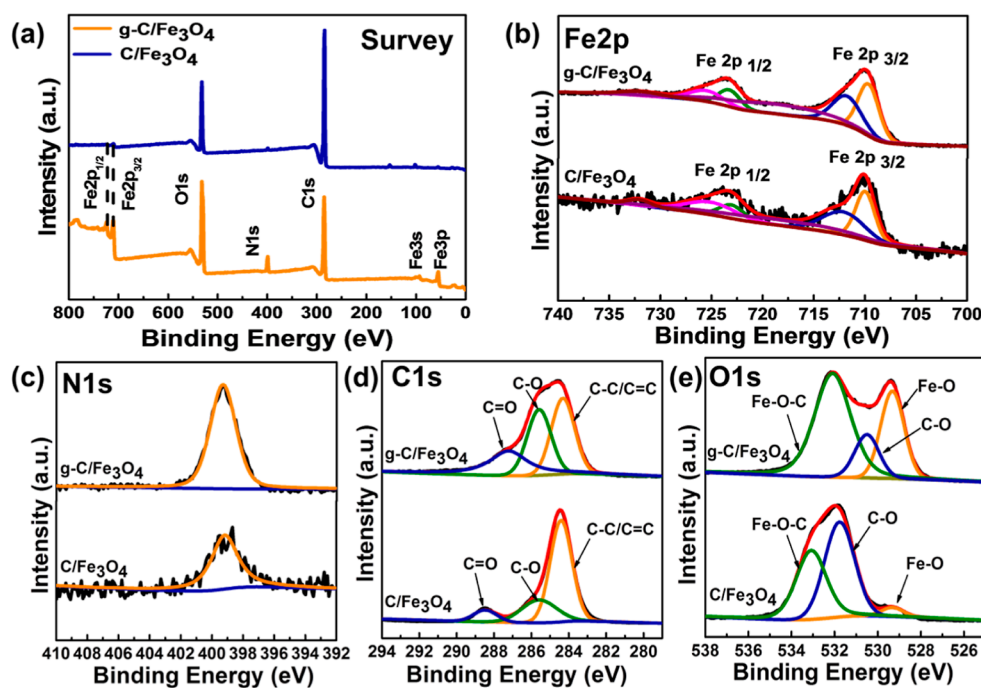
Figure 3. (a) Survey, (b) Fe 2p, (c) N 1s, (d) C 1s, and (e) O 1s core-level XPS spectra of C/Fe_3O_4 and $g\text{-}C/Fe_3O_4$ nanocomposites.

test conditions were that the time was 10 s and the speed was 1450 rpm. The four-ball machine is equipped with a vertical optical microscope and a spot automatic tester to measure the test of the steel ball grinding size, taking three tests, and the average grinding ball spot diameter value, respectively. As a result, its precision accuracy is 0.01 mm, and two measured ground spot diameter errors are less than 5%. Each test is duplicated three times.

3. RESULTS AND DISCUSSION

3.1. Characterization of C/Fe_3O_4 and $g\text{-}C/Fe_3O_4$ Nanocomposites. The synthesis schematic of $g\text{-}C/Fe_3O_4$ nanocomposites is illustrated in Figure 1. Specifically, the cassava starch was pretreated in a customized stirring ball mill, and the pretreated starch was dispersed in deionized water; then, EG and $FeCl_3$ were added to form a homogeneous yellow solution with stirring at 60 °C, followed by dropping aqueous ammonia, and then the above solution was heated in the reactor at 160 °C for 11 h under a N_2 atmosphere to obtain C/Fe_3O_4. Afterward, the mixture of C/Fe_3O_4 and PVP water solution was ball milled in a planetary ball mill for 5 h at 500 rpm. After that, the samples were washed and dried to obtain $g\text{-}C/Fe_3O_4$. Figure 2a presents the Raman spectra of C/Fe_3O_4 and $g\text{-}C/Fe_3O_4$ nanocomposites. It is clearly shown that C/Fe_3O_4 and $g\text{-}C/Fe_3O_4$ both had two characteristic bands at 1325.7 and 1559.6 cm^{-1}, which were assigned to the D- and G-bands of grapheme, respectively. The values of the intensity ratio of the D- and G-bands (I_D/I_G) can be indexed to estimate the graphitization degree. The I_D/I_G ratios of C/Fe_3O_4 and $g\text{-}C/Fe_3O_4$ were 1.52 and 0.87, respectively, suggesting orderly transformation of carbon from the chaotic layer structure to the graphite crystal structure. The result proved that the carbon in $g\text{-}C/Fe_3O_4$ was graphitized to a certain extent by ball milling, which was consistent with the literature reports.[28] The FT-IR spectrum of C/Fe_3O_4 (Figure 2b) showed a peak at 571 cm^{-1} that was attributed to the Fe–O bond, which indicated the presence of iron oxides.[34,35] The broad band at 3444 cm^{-1} was caused by the stretching vibration of –OH. The 1069,

1352, and 1117 cm^{-1} bands corresponded to the flexural vibration absorption peak of C–O–H. The peak at 1635 cm^{-1} belonged to the C=C vibration, which reflected the carbonization of starch.[36] The peak positions of C/Fe_3O_4 and $g\text{-}C/Fe_3O_4$ were almost the same, indicating that there was no breaking of the old bonds and the formation of new bonds; that is, no chemical reaction occurred during the ball milling process. Notably, the intensity of Fe–O and C–O–H bonds in $g\text{-}C/Fe_3O_4$ was enhanced compared with C/Fe_3O_4, which might be due to the oxidation of carbon and more exposure of Fe_3O_4 during ball milling.

The magnetic performance of C/Fe_3O_4 and $g\text{-}C/Fe_3O_4$ nanocomposites was measured by VSM, which was performed at room temperature with an implemented magnetic field of 20 kOe. As shown in Figure 2c, the magnetization–hysteresis curves of C/Fe_3O_4 and $g\text{-}C/Fe_3O_4$ nanocomposites were extremely coincident and exhibited nonlinear and reversible features with no hysteresis, which showed superparamagnetic performance. The saturation magnetization values (Ms) of C/Fe_3O_4 and $g\text{-}C/Fe_3O_4$ nanocomposites were 32.6 and 34.7 emu/g, respectively. The Ms value of $g\text{-}C/Fe_3O_4$ increased slightly, ascribing to the increase in Fe_3O_4 on the surface, which revealed that C/Fe_3O_4 and $g\text{-}C/Fe_3O_4$ nanocomposites had magnetization and superparamagnetism. The inline image at the bottom right showed the pictures of $g\text{-}C/Fe_3O_4$ scattered in rapeseed oil (Figure 2c). When the magnet was presented, the $g\text{-}C/Fe_3O_4$ nanocomposites could be quickly absorbed, indicating that $g\text{-}C/Fe_3O_4$ nanocomposites could be separated easily from rapeseed oil by magnetic decantation, which could effectively reduce the cost of waste oil recycling. Figure 2d shows the XRD patterns of C/Fe_3O_4 and $g\text{-}C/Fe_3O_4$ nanocomposites. Compared with the standard cards of Fe_3O_4 NPs (PDF #88-0866), C/Fe_3O_4 and $g\text{-}C/Fe_3O_4$ nanocomposites had the same peak position as that of Fe_3O_4, which showed the presence of Fe_3O_4 in the nanocomposites. In particular, $g\text{-}C/Fe_3O_4$ had an obvious and broad graphite
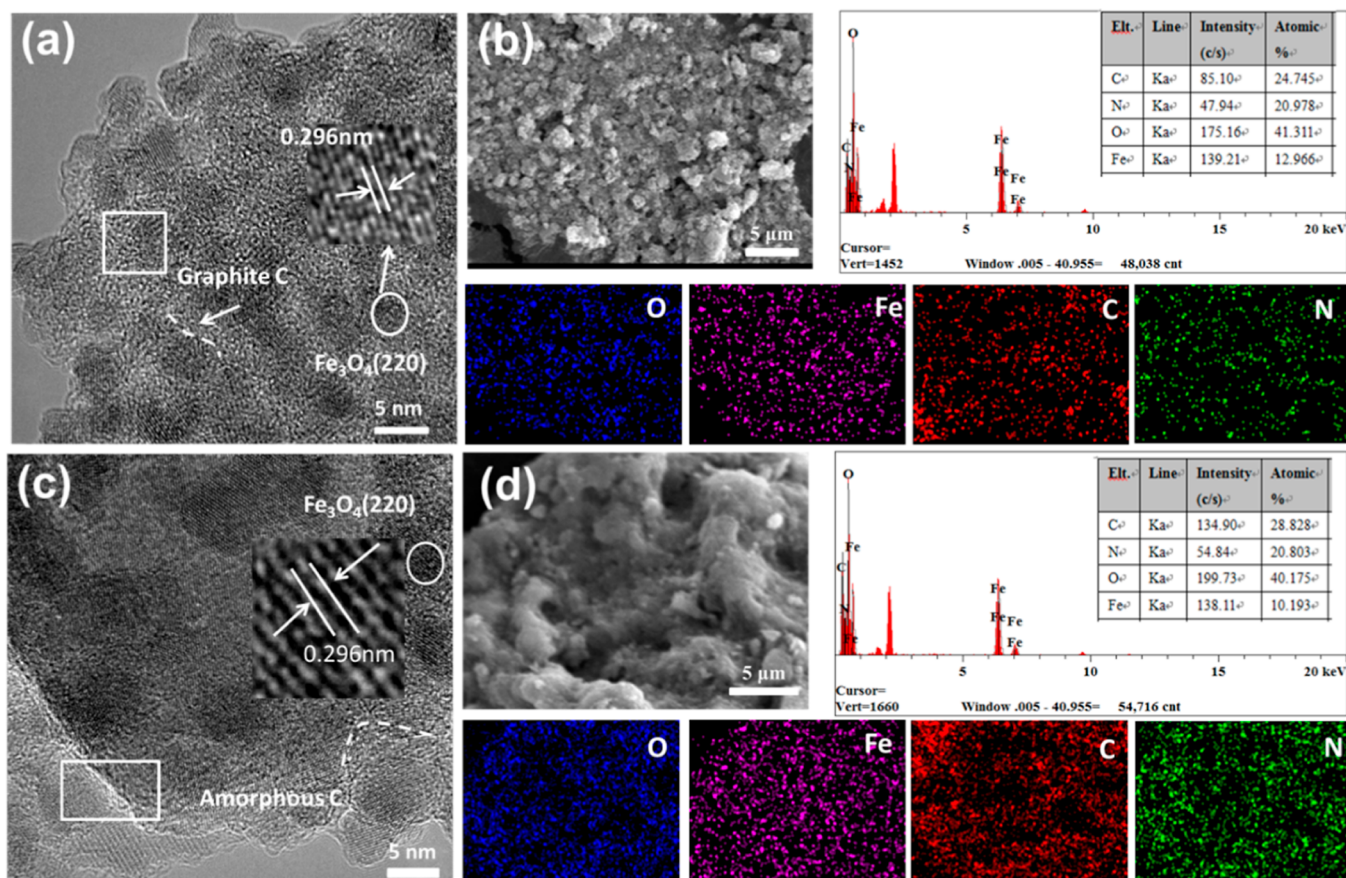
Figure 4. TEM images and SEM + EDS of (a,b) g-C/Fe$_3$O$_4$ and (c,d) C/Fe$_3$O$_4$.

diffraction peak at 20°, indicating graphitization of g-C/Fe$_3$O$_4$, which was consistent with Raman results.

XPS measurement was employed to investigate the surface chemical state of g-C/Fe$_3$O$_4$ and C/Fe$_3$O$_4$, the results are shown in Figure 3. In the full spectra of g-C/Fe$_3$O$_4$ and C/Fe$_3$O$_4$ (Figure 3a), the peaks of 710.1, 532.1, 399.1, and 285.1 eV corresponded to Fe 2p, O 1s, N 1s, and C 1s, respectively.[14] In the sub-spectrum for Fe 2p (Figure 3b), the spectra can be split into Fe 2p$_{3/2}$ and Fe 2p$_{1/2}$ peaks at 710.1 and 723.2 eV, corresponding to Fe^{2+}, as well as Fe 2p$_{3/2}$ and Fe 2p$_{1/2}$ peaks of Fe^{3+} at 712.4 and 725.6 eV, respectively.[14] The characteristic satellite peaks of Fe are also observed at the bonding energies of 718.9 and 732.0 eV. It is worth mentioning that the appearance of the N element was caused by the addition of ammonia during hydrothermal carbonization, and one peak of N 1s corresponded to N−H (Figure 3c). The C 1s XPS spectrum (Figure 3d) of the C/Fe$_3$O$_4$ showed three peaks corresponding to the chemical bands of C−C/C═C (284.4 eV), C−O (285.6 eV), and C═O/HO−C═O (288.5 eV), respectively.[35] Compared with C/Fe$_3$O$_4$, the C═O peak of g-C/Fe$_3$O$_4$ was shifted slightly to a lower binding energy, and the C−O and C═O peaks of g-C/Fe$_3$O$_4$ were enhanced significantly, which might be caused by the C atom obtaining electrons and graphitization occurring during the ball milling process. For g-C/Fe$_3$O$_4$, the intensity ratios of the C−C/C═C and C−O peaks decreased, revealing that the oxygen functional group increased and the carbon was oxidized slightly, in line with FT-IR results. The O 1s spectra (Figure 3e) of g-C/Fe$_3$O$_4$ and C/Fe$_3$O$_4$ showed that the peaks at 529.3, 531.8, and 533.1 eV corresponded to Fe−O, C−O, and

Fe−O−C, respectively.[37,38] The intensity of the Fe−O peak of g-C/Fe$_3$O$_4$ increased, suggesting that there were more iron oxides on the surface, which was consistent with the FT-IR and VSM results. Moreover, the C and Fe contents of C/Fe$_3$O$_4$ and g-C/Fe$_3$O$_4$ were very similar (~19.0% and ~39.0 wt%, respectively, Table S1). The particle sizes of C/Fe$_3$O$_4$ and g-C/Fe$_3$O$_4$ were 715.9 and 580.6 nm (Table S1), respectively, which implied that the ball milling process could effectively reduce the size of nanocomposites.

In addition, high-resolution SEM (EDS) and TEM analyses were performed to analyze the interpenetrating network structure and other effects of ball milling. As shown in Figure S1, the carbon layer and spherical Fe$_3$O$_4$ interweaved to form an interpenetrating network structure, and the structure was not destroyed before or after ball milling. There is a clear nanocrystalline structure of Fe$_3$O$_4$ in g-C/Fe$_3$O$_4$ and C/Fe$_3$O$_4$ (Figure 4a,c), and the lattice fringes with a d-lattice spacing of 0.296 nm were in agreement with those of the (220) crystal planes of Fe$_3$O$_4$. Moreover, it can be seen clearly that the interface between Fe$_3$O$_4$ and carbon disappeared after ball milling, indicating that ball milling could effectively eliminate the interface effect. As shown in Figures 4b,d and S1, the SEM images showed that the size of g-C/Fe$_3$O$_4$ was significantly smaller than that of C/Fe$_3$O$_4$, revealing that ball milling could reduce the particle size of the nanocomposites, which was consistent with the reported literature results.[39] The Fe, C, O, and N element EDS images of g-C/Fe$_3$O$_4$ and C/Fe$_3$O$_4$ confirmed the uniform distribution of Fe$_3$O$_4$-rich regions on the carbon. The element distribution of g-C/Fe$_3$O$_4$ was more uniform than that of C/Fe$_3$O$_4$, it can be used to predict that
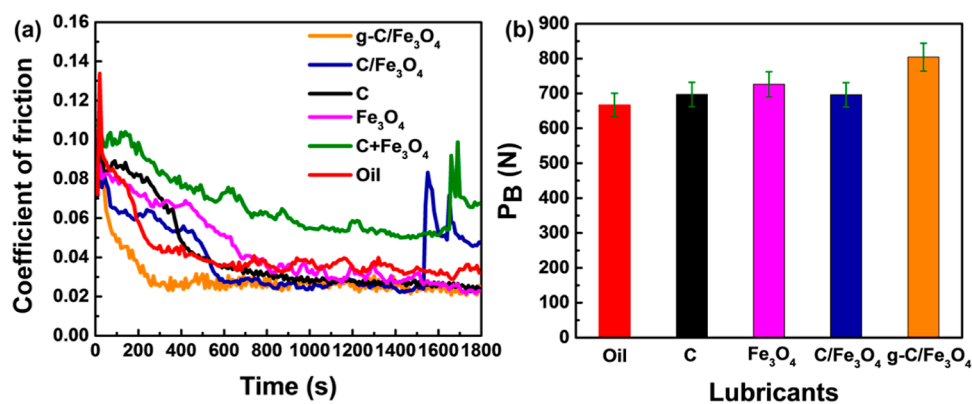
Figure 5. (a) COF and (b) extreme pressure of rapeseed oil, g-C/Fe$_3$O$_4$, and other control samples.

the dispersibility of g-C/Fe$_3$O$_4$ was improved during ball milling.

From the above results, we can infer the possible graphitization mechanism of the C/Fe$_3$O$_4$ nanocomposite during the ball milling process. The C/Fe$_3$O$_4$ nanocomposites rotated at a high speed in the planetary ball mill and were continuously collided with by the zirconium balls. The large block was cut into small fragments by mechanical force and then peeled off to form smaller particles. At the same time, the grinding ball rolled along the jar surface in a series of parallel layers to convert mechanical energy into internal energy; afterward, the internal energy was transferred to the powder to make part of the amorphous carbon undergo phase transformation. Meanwhile, a graphitic carbon layer was formed under mechanical force. In addition, graphitized carbon, Fe$_3$O$_4$, and most of the amorphous carbon were redistributed and rearranged at high rotational speeds, resulting in a more ordered and uniform plane.

3.2. Tribological Performances. The tribological performances of the g-C/Fe$_3$O$_4$ and the control samples, including C/Fe$_3$O$_4$, hydrothermal carbon, Fe$_3$O$_4$ NPs, and C + Fe$_3$O$_4$ (the mixture of hydrothermal carbon and Fe$_3$O$_4$ NPs), were investigated at 392 N, a temperature of 155 °C, and a concentration of 0.3 wt%, and the results are shown in Figure 5a. The coefficient of friction (COF) value of the C/Fe$_3$O$_4$ was 0.040 at 600 s, demonstrating a good lubricating effect, however, the lubricating effect was unstable when the friction time increased. The COF values of control samples, including hydrothermal carbon, Fe$_3$O$_4$ NPs, and C + Fe$_3$O$_4$, were 0.040, 0.044, and 0.068, respectively, which showed an unsatisfactory lubricating effect. Therefore, it was deduced that the good lubricating effect originated from the interpenetrating network structure of C/Fe$_3$O$_4$ and a synergistic effect between hydrothermal carbon and Fe$_3$O$_4$. Encouragingly, the COF value of g-C/Fe$_3$O$_4$ was 0.029 at 200 s and remained constant over a long friction time, which showed excellent tribological properties. The satisfactory lubricating effect was probably attributed to the graphitization and good dispersibility (Figure S2, only a spot of delamination was observed after 96 h of placement) of g-C/Fe$_3$O$_4$ nanocomposites. That is, the two-dimensional lamellar structure of graphitized carbon was easier to enter the friction interface to make the g-C/Fe$_3$O$_4$ smoothly distributed on the friction surface, and the tight interweaving of Fe$_3$O$_4$ and carbon overcame the structural rupture caused by friction, thus demonstrating an outstanding lubricating effect. The optical photographs of the g-C/Fe$_3$O$_4$ and the control samples' wear spots on steel balls are shown in Figure S3. The

g-C/Fe$_3$O$_4$ showed the smallest WSD, which indicated effectively reduced wear. As shown in Table S2, compared with other Fe$_3$O$_4$-based nanomaterials, g-C/Fe$_3$O$_4$ presented remarkable lubricating performance under high load and high temperature, showing great potential in practical application for high-temperature tribology. Furthermore, the extreme pressure performance of the g-C/Fe$_3$O$_4$ and the control samples, including C/Fe$_3$O$_4$, hydrothermal carbon, and Fe$_3$O$_4$ NPs, was also studied. As shown in Figure 5b, adding C, Fe$_3$O$_4$, and C/Fe$_3$O$_4$ into the rapeseed oil could improve the P_B value of rapeseed oil (667 N), and the P_B values were 697, 726, and 696 N, respectively. The P_B value of C/Fe$_3$O$_4$ was lower than that of C and Fe$_3$O$_4$, which may be related to its poor dispersibility in rapeseed oil. Surprisingly, g-C/Fe$_3$O$_4$ showed the largest extreme pressure value, which was 804 N. It clearly indicated that g-C/Fe$_3$O$_4$ showed good stability under extreme pressure, attributable to its interpenetrating network structure and graphitization.

To further investigate the anti-friction properties of g-C/Fe$_3$O$_4$, we investigated the effect of different temperatures, different concentrations, and different applied loads on its properties, the results are shown in Figure S4. As displayed in Figure S4a, the COF of g-C/Fe$_3$O$_4$ decreased with increasing temperatures, and the lowest COF value was 0.048 at 175 °C. This might be related to the graphitization transition of carbon at a high temperature. However, there is a large, unstable fluctuation in the friction coefficient at 175 °C, which might be caused by the decrease in the oil phase viscosity at a high temperature. Based on this, the preferred temperature was 155 °C. Figure S4b shows the changes in the friction coefficient with the various concentrations of g-C/Fe$_3$O$_4$. When adding 0.3 wt% g-C/Fe$_3$O$_4$, the friction coefficient curve tended to be smooth and stable over a long friction time. Meanwhile, the COF of 0.3 wt% g-C/Fe$_3$O$_4$ reached the lowest (0.049). However, when the concentration was less than 0.3 wt%, not enough particles participated in lubrication, resulting in a poor lubrication effect. As the concentration of g-C/Fe$_3$O$_4$ exceeded 0.3 wt%, the COF increased slightly, which was attributed to their agglomeration to form abrasive particles, leading to jamming in the process of friction. Therefore, the g-C/Fe$_3$O$_4$ concentration of 0.3 wt% was considered as an appropriate value. As shown in Figure S4c, the friction coefficient decreased first and then increased with the increase in the applied load. The reason for this trend was the potential of nanocomposite decomposition under high loading forces. When the load was 392 N, the average COF of g-C/Fe$_3$O$_4$ was 0.029. Therefore, we can conclude that the optimal
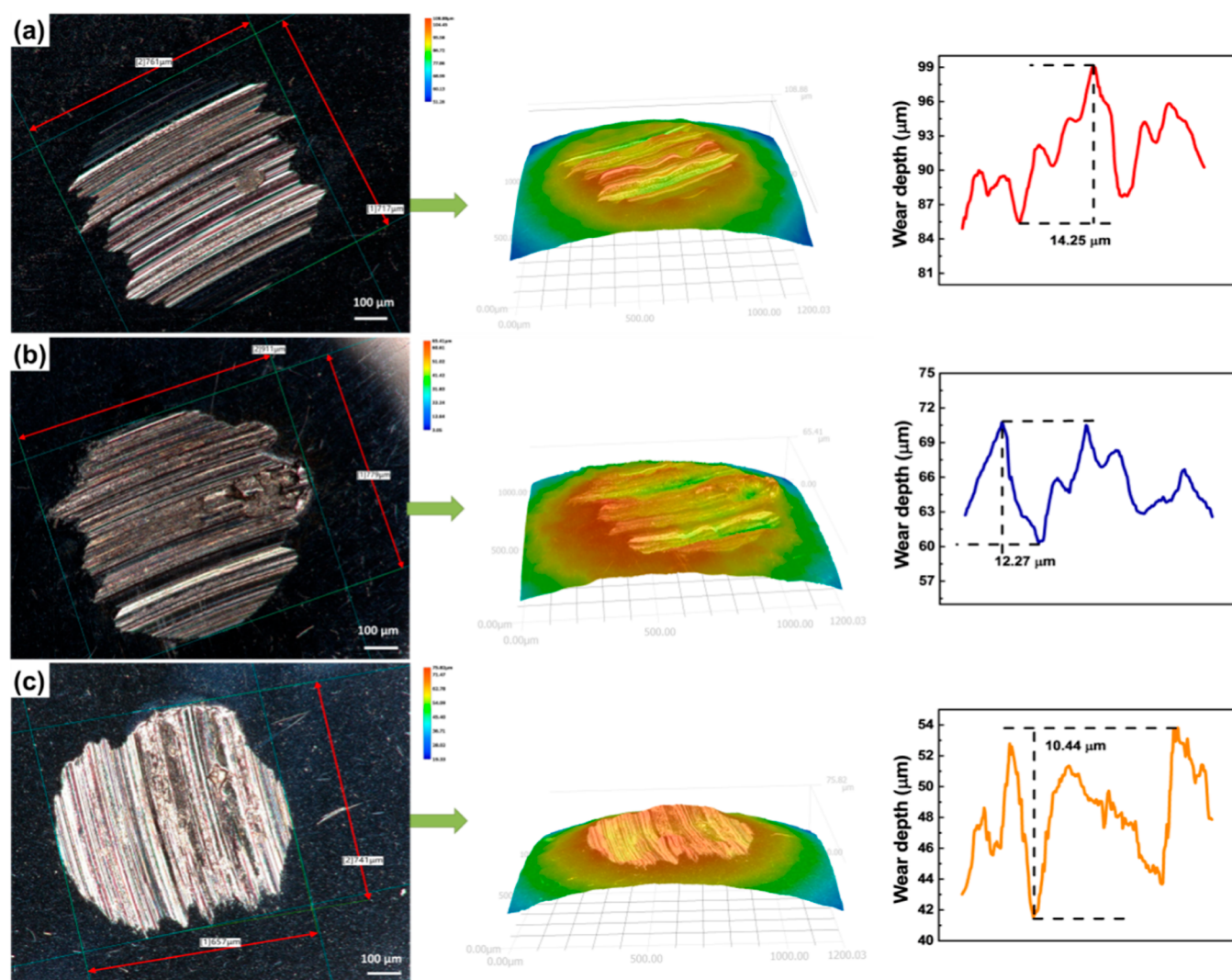
Figure 6. Optical photographs of worn surfaces and the three-dimensional profile of the wear track of the steel ball after friction tests (at 392 N, 155 °C, 0.3 wt%): (a) pure rapeseed oil, (b) C/Fe$_3$O$_4$, and (c) g-C/Fe$_3$O$_4$.

lubrication conditions for g-C/Fe$_3$O$_4$ were 155 °C, 0.3 wt%, and 392 N.

To illustrate the excellent lubricating performance of g-C/Fe$_3$O$_4$ under high temperature and high load, the effect of different load forces on the lubricating performance of g-C/Fe$_3$O$_4$ and the control samples, including C/Fe$_3$O$_4$, hydrothermal carbon, Fe$_3$O$_4$ NPs, and C + Fe$_3$O$_4$, was explored under 155 °C, and the results are shown in Figure S5. Pure Fe$_3$O$_4$ could still operate under high load, but its friction coefficient always maintained a relatively large trend. Pure hydrothermal carbon showed better friction performance when the load force was lower than 686 N, which is related to the carbon film formed. With the increase in loading force, the carbon film was destroyed and lost its anti-friction effect at 882 N. Compared with Fe$_3$O$_4$, hydrothermal carbon, and C + Fe$_3$O$_4$, the C/Fe$_3$O$_4$ and g-C/Fe$_3$O$_4$ nanocomposites showed good lubricating properties ascribing to their interpenetrating network structure under 155 °C and 882 N. Figure S4e shows that the COF of g-C/Fe$_3$O$_4$ was run smoothly after a long friction time compared with that of C/Fe$_3$O$_4$ at 882 N, which might be attributed to the synergistic anti-friction advantage of the graphitized carbon and the interpenetrating network structure in g-C/Fe$_3$O$_4$. When the load force increased to

980 N (Figure S5f), the COF of g-C/Fe$_3$O$_4$ was smaller than that of C/Fe$_3$O$_4$, and it could almost run smoothly, while C/Fe$_3$O$_4$ showed an unstable state, which indicated that the interpenetrating network structure of C/Fe$_3$O$_4$ was damaged. Therefore, we can conclude that g-C/Fe$_3$O$_4$ had a better lubricating effect than C/Fe$_3$O$_4$ under high temperature and high pressure, attributable to the graphitized carbon and interpenetrating network structure.

3.3. Surface Analysis. Figure 6 shows the three-dimensional profile of the wear scar lubricated with g-C/Fe$_3$O$_4$, C/Fe$_3$O$_4$, and pure oil under optimal conditions. As shown in Figure 6, the values of the wear scar width lubricated with pure rapeseed oil and the C/Fe$_3$O$_4$ nanocomposite exhibited 740 and 840 μm, respectively. In contrast, the wear width was decreased to 690 μm when lubricated by g-C/Fe$_3$O$_4$. The values of wear scar depth lubricated with pure rapeseed oil, C/Fe$_3$O$_4$, and g-C/Fe$_3$O$_4$ nanocomposites exhibited 14.25, 12.27, and 10.44 μm, respectively. Hence, when adding g-C/Fe$_3$O$_4$ into rapeseed oil, the wear scar width and depth were reduced by 6.8 and 26.7%, respectively, and displayed comparatively slight furrows compared to the pure rapeseed oil, which revealed that the g-C/Fe$_3$O$_4$ nanocomposite showed better anti-friction and anti-wear properties than C/Fe$_3$O$_4$. Fur-
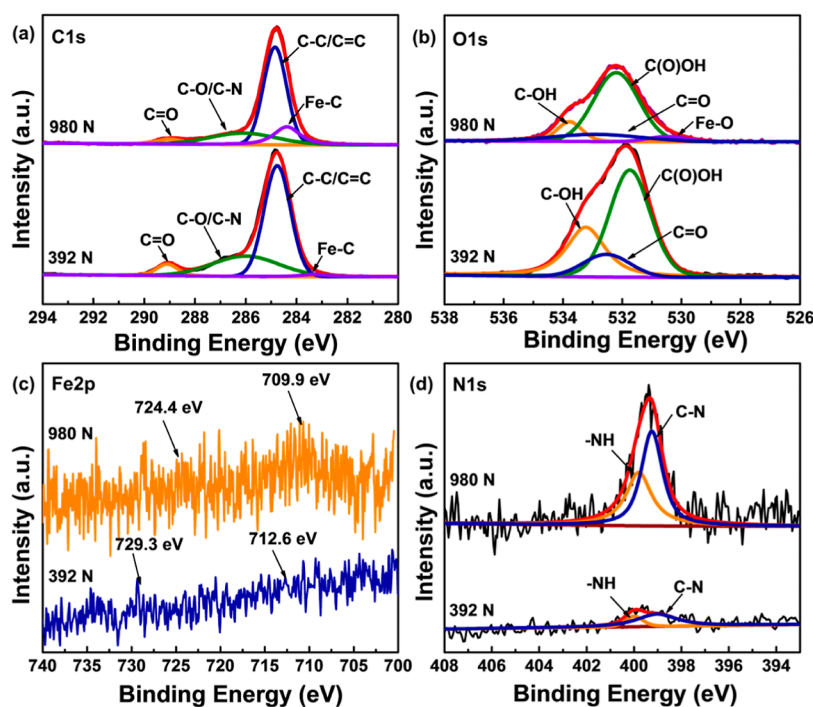
Figure 7. XPS spectra of (a) C 1s, (b) O 1s, (c) Fe 2p, and (d) N 1s on the surface of the wear scar lubricated with 0.3 wt% g-C/Fe$_3$O$_4$ at 392 and 980 N at 155 °C for 30 min.

thermore, the SEM + EDS (Figure S6) showed the wear scar morphology and element distribution after the rapeseed oil, C/Fe$_3$O$_4$, and g-C/Fe$_3$O$_4$ lubrication. From the SEM images, rapeseed oil and C/Fe$_3$O$_4$ showed deep and wide wear scars with more iron filings remaining on the surface, while g-C/Fe$_3$O$_4$ showed shallow wear scars and a smooth surface. Moreover, the EDS element distribution mapping images showed that Fe, C, and O had a relatively uniform distribution on the g-C/Fe$_3$O$_4$ wear scar. The above result also verified that g-C/Fe$_3$O$_4$ had a better lubrication effect than C/Fe$_3$O$_4$.

3.4. Friction and Wear Mechanism Analysis. To understand the lubrication mechanism, further investigations were conducted. The Raman spectrum of the wear tracks (Figure S7) showed the characteristic peaks of graphitic carbon (D-band at 1392 cm^{-1} and G-band at 1582 cm^{-1}) and α-FeOOH (671 cm^{-1}).[2] The I_D/I_G ratio of g-C/Fe$_3$O$_4$ after friction was 0.68 at 392 N, which suggested that further graphitization occurred during the friction process. The G-band peak shape was high and narrow, indicating that the graphene produced by friction had a good crystal shape. The D-band had a large and short broadband and an asymmetric shape, indicating that there was a small amount of mixture of amorphous and crystalline states.[40] The α-FeOOH at 671 cm^{-1} was the antisymmetric stretching vibration of the single-bridge oxygen of six-coordinated iron, and the relatively weak broad peak was attributed to the weak oxidation of the friction surface, which might be affected by the air humidity. In the Raman spectrum, the signal of crystalline carbon was the strongest, while the signal of Fe$_3$O$_4$ did not appear, indicating that the friction surface formed a carbon film by the deposited graphitic carbon at 392 N, while no friction film was formed. The results indicated that g-C/Fe$_3$O$_4$ with the interpenetrating network structure can easily enter the friction pair, hence providing carbon films on the rubbing surfaces to reduce wear during the friction process. At 980 N, the absorption peak of α-

FeOOH was enhanced, indicating that more Fe$_3$O$_4$ was involved in friction from a Fe$_3$O$_4$ tribofilm. Meanwhile, the D-band was split into two sharp and weak peaks, which indicated that the graphitized carbon in g-C/Fe$_3$O$_4$ was destroyed under 980 N. These phenomena suggested that the carbon film and the Fe$_3$O$_4$ tribofilm synergistically played an anti-friction effect under high load.

To ascertain the composition of tribofilms formed on the worn surface, the elemental chemical state of the worn surface of the steel ball lubricated with g-C/Fe$_3$O$_4$ was investigated using XPS. Figure 7 shows the curve-fitted spectra of C 1s, O 1s, N 1s, and Fe 2p under 392 and 980 N. As shown in Figure 7a, the C═O, C─O/C─N, and C─C/C═C signals might be derived from the graphitic carbon or rapeseed oil. Under 392 N, the weak Fe─C signal was derived from a slight wear of the friction pair. Additionally, the absence of the Fe─O signal further verified that the structure of Fe$_3$O$_4$ was not destroyed (Figure 7b), facilitating the recovery of g-C/Fe$_3$O$_4$ from waste oil. In this environment, the sliding of g-C/Fe$_3$O$_4$ nanocomposites and the deposited carbon film may together play an anti-wear and anti-friction effect. Two weak satellite peaks of the Fe 2p XPS spectrum (Figure 7c) can be detected at 729.3 and 712.6 eV, which correspond to Fe 2p$_{1/2}$ and Fe 2p$_{3/2}$, respectively. The peak at 712.6 eV represented the FeO, which might have arisen from the oxidized friction pair surface. The peak at 729.3 eV was assigned to the purely physical iron filings on the friction pair surface. The N 1s spectrum (Figure 7d) showed two signal peaks at 400.1 and 399.2 eV, corresponding to ─NH and C─N, respectively. These results showed that the main anti-friction effect was the carbon film deposited on the worn surface under 392 N, and Fe$_3$O$_4$ could almost maintain its complete structure without damage. In other words, g-C/Fe$_3$O$_4$ could still maintain its complete structure and also highlight the excellent anti-friction and anti-wear due to the interpenetrating network structure at a high temperature.
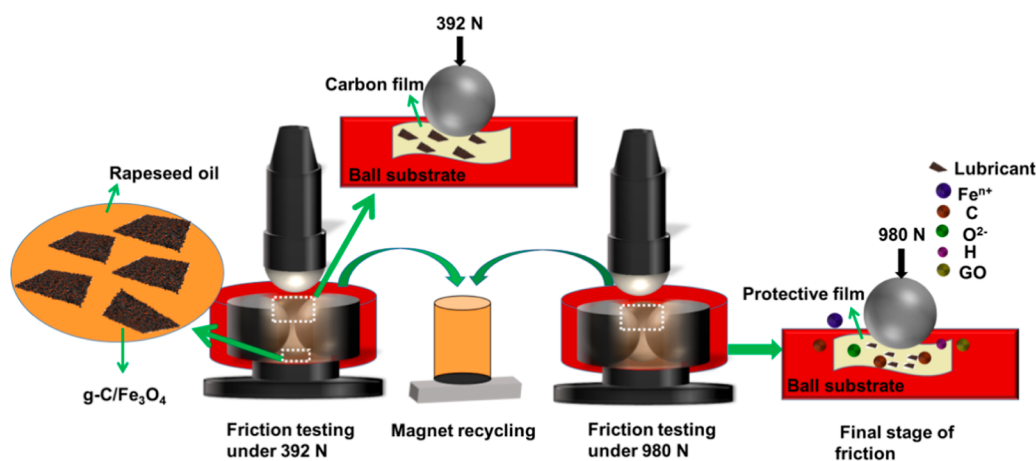
Figure 8. Schematic of the rapeseed oil with g-C/Fe$_3$O$_4$ nanocomposites in friction from low load to high load at 155 °C.

Under 980 N, as shown in Figure 7a, the Fe—C signal peak was significantly enhanced, indicating that more g-C/Fe$_3$O$_4$ was involved in the lubrication of the friction pair surface, which was consistent with the Raman results. Interestingly, the O 1s spectrum (Figure 7b) reflected four peaks at 530.5, 532.2, 532.9, and 533.8 eV.[41] Among them, the peak at 530.5 eV was assigned to the anionic oxygen in Fe$_2$O$_3$ and Fe$_3$O$_4$, and other peaks belonged to C(O)OH (532.2 eV), C=O (532.9 eV), and C—OH (533.8 eV). In the Fe 2p spectrum (Figure 7c), the signal peaks at 709.9 and 724.4 eV belonged to Fe^{2+} (2p$_{3/2}$) and Fe^{3+} (2p$_{1/2}$), respectively. The Fe^{2+} and Fe^{3+} peaks showed the existence of Fe$_2$O$_3$ and Fe$_3$O$_4$, which came from the g-C/Fe$_3$O$_4$ tribofilm and the steel ball, respectively. Thus, we can conclude that a physicochemical reaction will occur on the friction surface under 980 N, and a protective film composed of a carbon film, a g-C/Fe$_3$O$_4$ friction film, and a chemical reaction film will be formed to achieve an excellent lubrication effect.

Based on the above results, the schematic of the rapeseed oil with g-C/Fe$_3$O$_4$ nanocomposites in the friction process was proposed in Figure 8. Initially, the g-C/Fe$_3$O$_4$ could rapidly enter the interfaces of the rubbing surfaces. Under low load force, it can rely on the sliding of the g-C/Fe$_3$O$_4$ and the deposited carbon film to play a frictional role, while the structure of the g-C/Fe$_3$O$_4$ was not damaged, and a relatively complete g-C/Fe$_3$O$_4$ can be obtained during the recovery of waste oil. As the load increased, the g-C/Fe$_3$O$_4$ friction film was generated, which formed a protective film on the friction surface together with the carbon film and other chemical reaction films containing Fe$_3$O$_4$, Fe$_2$O$_3$, FeO, FeOOH, and GO. The deposition of the g-C/Fe$_3$O$_4$ nanocomposites rapidly filled in the grooves, resulting in a smooth and shallow worn surface and preventing the direct asperity contact of two rubbing surfaces. Due to the interpenetrating network structure of g-C/Fe$_3$O$_4$, g-C/Fe$_3$O$_4$ was more uniformly dispersed on the friction surface, which showed superior stability and outstanding lubricating performance compared to the core—shell nanocomposites under high temperature and high load. Furthermore, the presence of graphitic carbon in g-C/Fe$_3$O$_4$ can effectively promote the carbon film to be generated while remaining for a long time during the friction process, thus demonstrating that g-C/Fe$_3$O$_4$ exhibited better tribological performance than C/Fe$_3$O$_4$.

4. CONCLUSIONS

To summarize, an in situ hydrothermal carbonization method combined with a subsequent ball milling process at room temperature has been developed to prepare the graphitized and interpenetrating network structure of g-C/Fe$_3$O$_4$. As a result, the effects of ball milling could be summarized as follows: generating graphitized carbon, reducing particle size, eliminating interface effects, and improving dispersibility. Moreover, g-C/Fe$_3$O$_4$ used as a lubricant additive in rapeseed oil exhibited excellent tribological properties including extreme pressure up to 804 N and a low friction coefficient as low as 0.029 under 155 °C. The lubricating behavior of g-C/Fe$_3$O$_4$ under low load was mainly due to its interpenetrating network structure and graphitized carbon, while under high load, it is manifested as the synergistic effect of the carbon film and Fe$_3$O$_4$ film. These findings may pave a new way for the design and fabrication of lubricant additives with excellent tribological performance under high temperature and high load.

■ ASSOCIATED CONTENT

ⓢ Supporting Information

The Supporting Information is available free of charge at https://pubs.acs.org/doi/10.1021/acsami.2c03468.

> High-resolution SEM images and dispersibility of C/Fe$_3$O$_4$ and g-C/Fe$_3$O$_4$, optical photographs of the g-C/Fe$_3$O$_4$ and the control samples dispersions in rapeseed oil after rubbing, influence of different parameters on the friction coefficient, variation of the friction coefficient with different applied loads of g-C/Fe$_3$O$_4$, SEM + EDS images and Raman spectra of g-C/Fe$_3$O$_4$ after rubbing, and element content of C/Fe$_3$O$_4$ and g-C/Fe$_3$O$_4$ (PDF)

■ AUTHOR INFORMATION

Corresponding Authors

Huayu Hu — *School of Chemistry and Chemical Engineering, Guangxi University, Nanning 510004, China*; Phone: +86-771-3233718; Email: yuhuahu@163.com; Fax: +86-771-3233718

Tao Gan — *School of Chemistry and Chemical Engineering, Guangxi University, Nanning 510004, China; Fine Chemical Industry Research Institute, School of Chemistry, Sun Yat-sen University, Guangzhou 510275, China*; ⓞ orcid.org/0000-0001-5077-3296; Phone: +86-771-3233718; Email: gant@gxu.edu.cn; Fax: +86-771-3233718

Authors

Yuying Chen — *School of Chemistry and Chemical Engineering, Guangxi University, Nanning 510004, China*

Qing Yang — *School of Chemistry and Chemical Engineering, Guangxi University, Nanning 510004, China*

Wenqin Lu — *School of Chemistry and Chemical Engineering, Guangxi University, Nanning 510004, China*

Yanjuan Zhang — *School of Chemistry and Chemical Engineering, Guangxi University, Nanning 510004, China;* ⓘ orcid.org/0000-0001-8206-6051

Zuqiang Huang — *School of Chemistry and Chemical Engineering, Guangxi University, Nanning 510004, China;* ⓘ orcid.org/0000-0003-0727-8016

Complete contact information is available at:
https://pubs.acs.org/10.1021/acsami.2c03468

■ REFERENCES

(1) Wang, J.; Zhuang, W.; Liang, W.; Yan, T.; Li, T.; Zhang, L.; Li, S. Inorganic Nanomaterial Lubricant Additives for Base Fluids, to Improve Tribological Performance: Recent Developments. *Friction* **2021**, *10*, 645−676.

(2) Zhao, J.; Li, Y.; He, Y.; Luo, J. In Situ Green Synthesis of the New Sandwich-Like Nnanostructure of Mn₃O₄/graphene as Lubricant Additives. *ACS Appl. Mater. Interfaces* **2019**, *11*, 36931−36938.

(3) Song, H.; Wang, Z.; Yang, J.; Jia, X.; Zhang, Z. Facile Synthesis of Copper/Polydopamine Functionalized Graphene Oxide Nanocomposites with Enhanced Tribological Performance. *Chem. Eng. J.* **2017**, *324*, 51−62.

(4) Liu, L.; Jiao, S.; Peng, Y.; Zhou, W. A Green Design for Lubrication: Multifunctional System Containing Fe₃O₄@MoS₂ Nanohybrid. *ACS Sustainable Chem. Eng.* **2018**, *6*, 7372−7379.

(5) Ari-Gur, P.; Sariel, J.; Stanford, M. K.; DellaCorte, C.; Abel, P. B. Phase Identification of Hard Precipitates in PS304 Coatings. *Surf. Eng.* **2011**, *27*, 196−198.

(6) Wang, H.; Yan, L.; Liu, D.; Wang, C.; Zhu, Y.; Zhu, J. Investigation of the Tribological Properties: Core-Shell Structured Magnetic Ni@NiO Nanoparticles Reinforced Epoxy Nanocomposites. *Tribol. Int.* **2015**, *83*, 139−145.

(7) Tian, X.; Qiao, H.; Chu, X. Wear Performance of Bonded Composite Coatings under Dry Sliding. *Surf. Coat. Technol.* **2014**, *240*, 191−196.

(8) Song, X.; Qiu, Z.; Yang, X.; Gong, H.; Zheng, S.; Cao, B.; Wang, H.; Möhwald, H.; Shchukin, D. Submicron-Lubricant Based on Crystallized Fe₃O₄ Spheres for Enhanced Tribology Performance. *Chem. Mater.* **2014**, *26*, 5113−5119.

(9) Zhang, Q.; Wu, B.; Song, R.; Song, H.; Zhang, J.; Hu, X. Preparation, Characterization and Tribological Properties of Poly-alphaolefin with Magnetic reduced Graphene Oxide/Fe₃O₄. *Tribol. Int.* **2020**, *141*, 105952.

(10) Yang, M.; Fan, S.; Huang, H.; Zhang, Y.; Huang, Z.; Hu, H.; Liang, J. In-Situ Synthesis of Calcium Borate/Cellulose Acetate-Laurate Nanocomposite as Efficient Extreme Pressure and Anti-Wear Lubricant Additives. *Int. J. Biol. Macromol.* **2020**, *156*, 280−288.

(11) Du, Z.; Qiu, Y.; Niu, T.; Wang, W.; Ye, X.; Wang, J.; Zhang, W. L.; Choi, H. J.; Zeng, H. Bio-Inspired Passion Fruit-Like Fe₃O₄@C Nanospheres Enabling High-Stability Magnetorheological Performances. *Langmuir* **2020**, *36*, 7706−7714.

(12) An, R.; Wu, M.; Li, J.; Qiu, X.; Shah, F. U.; Li, J. On the Ionic Liquid Films 'pinned' by Core-Shell Structured Fe₃O₄@Carbon Nanoparticles and Their Tribological Properties. *Phys. Chem. Chem. Phys.* **2019**, *21*, 26387−26398.

(13) Xu, Y.; Geng, J.; Peng, Y.; Liu, Z.; Yu, J.; Hu, X. Lubricating Mechanism of Fe₃O₄@MoS₂ Core-Shell Nanocomposites as Oil Additives for Steel/Steel Contact. *Tribol. Int.* **2018**, *121*, 241−251.

(14) Zhao, Q.; Liu, J.; Wang, Y.; Tian, W.; Liu, J.; Zang, J.; Ning, H.; Yang, C.; Wu, M. Novel In-Situ Redox Synthesis of Fe₃O₄/rGO Composites with Superior Electrochemical Performance for Lithium-Ion Batteries. *Electrochim. Acta* **2018**, *262*, 233−240.

(15) Sammaiah, A.; Huang, W.; Wang, X. Synthesis of Magnetic Fe₃O₄/Graphene Oxide Nanocomposites and Their Tribological Properties under Magnetic Field. *Mater. Res. Express* **2018**, *5*, 105006.

(16) Huang, J.; Li, Y.; Jia, X.; Song, H. Preparation and Tribological Properties of Core-Shell Fe₃O₄@C Microspheres. *Tribol. Int.* **2019**, *129*, 427−435.

(17) Zhang, L.; Pu, J.; Wang, L.; Xue, Q. Frictional Dependence of Graphene and Carbon Nanotube in Diamond-Like Carbon/Ionic Liquids Hybrid Films in Vacuum. *Carbon* **2014**, *80*, 734−745.

(18) Sammaiah, A.; Dai, Q.; Huang, W.; Wang, X. Synthesis of GO-Fe₃O₄-Based Ferrofluid and its Lubrication Performances. *Proc. Inst. Mech. Eng., Part J* **2020**, *234*, 1160−1167.

(19) Duan, C.; Gao, C.; Li, S.; Yang, R.; Yang, Z.; Zhang, Y.; Tao, L.; Zhang, X.; Wang, Q.; Wang, T. Tailoring Polyimide Composites with Low Friction and Wear at High Temperatures. *J. Appl. Polym. Sci.* **2022**, *139*, 51736.

(20) Singh, A. K.; Shukla, N.; Verma, D. K.; Kavita; Kumar, B.; Rastogi, R. B. Enhancement of Triboactivity of Nanolamellar Graphitic-C₃N₄ by N-Doped ZnO Nanorods. *Ind. Eng. Chem. Res.* **2021**, *60*, 864−874.

(21) Wu, X.; Gong, K.; Zhao, G.; Lou, W.; Wang, X.; Liu, W. Mechanical Synthesis of Chemically Bonded Phosphorus-Graphene Hybrid as High-Temperature Lubricating Oil Additive. *RSC Adv.* **2018**, *8*, 4595−4603.

(22) Wang, Y.; Gao, K.; Zhang, B.; Wang, Q.; Zhang, J. Structure Effects of sp²-Rich Carbon Films under Super-Low Friction Contact. *Carbon* **2018**, *137*, 49−56.

(23) Jiang, F.; Yao, Y.; Natarajan, B.; Yang, C.; Gao, T.; Xie, H.; Wang, Y.; Xu, L.; Chen, Y.; Gilman, J.; et al. Ultrahigh-Temperature Conversion of Biomass to Highly Conductive Graphitic Carbon. *Carbon* **2019**, *144*, 241−248.

(24) Li, Y.; Hu, J.; Wang, Z.; Yang, K.; Huang, W.; Cao, B.; Li, Z.; Zhang, W.; Pan, F. Low-Temperature Catalytic Graphitization to Enhance Na-Ion Transportation in Carbon Electrodes. *ACS Appl. Mater. Interfaces* **2019**, *11*, 24164−24171.

(25) Liu, C.; Liu, X.; Tan, J.; Wang, Q.; Wen, H.; Zhang, C. Nitrogen-Doped Graphene by All-Solid-State Ball-Milling Graphite with Urea as a High-Power Lithium Ion Battery Anode. *J. Power Sources* **2017**, *342*, 157−164.

(26) Jin, X.; He, R.; Dai, S. Electrochemical Graphitization: An Efficient Conversion of Amorphous Carbons to Nanostructured Graphites. *Chem.—Eur. J.* **2017**, *23*, 11455−11459.

(27) Fan, Q.; Noh, H.; Wei, Z.; Zhang, J.; Lian, X.; Ma, J.; Jung, S.; Jeon, I.; Xu, J.; Baek, J. Edge-Thionic Acid-Functionalized Graphene Nanoplatelets as Anode Materials for High-Rate Lithium Ion Batteries. *Nano Energy* **2019**, *62*, 419−425.

(28) Zhang, R.; Li, Y. Structures and High Temperature Frictional Behaviors of Coal Pitch-Derived Carbonaceous Mesophases (CMs) Ball Milled for Different Durations. *Tribol. Lett.* **2008**, *32*, 209−213.

(29) He, D.; Cai, M.; Yan, H.; Lin, Q.; Fan, X.; Zhang, L.; Zhu, M. Tribological Properties of $Ti_3C_2T_x$ MXene Reinforced Interpenetrating Polymers Network Coating. *Tribol. Int.* **2021**, *163*, 107196.

(30) Wang, X.; Fang, X.; Liu, X.; et al. Formation of Unique Three-Dimensional Interpenetrating Network Structure with a Ternary Composite. *J. Mater. Sci.: Mater. Electron.* **2018**, *29*, 18699−18707.

(31) Zhang, H.; Sun, X. H.; Hubbe, M. A.; Pal, L. Highly Conductive Carbon Nanotubes and Flexible Cellulose Nanofibers Composite Membranes with Semi-Interpenetrating Networks Structure. *Carbohydr. Polym.* **2019**, *222*, 115013.

(32) Liao, Z.; Huang, Z.; Hu, H.; Zhang, Y.; Tan, Y. Microscopic Structure and Properties Changes of Cassava Stillage Residue Pretreated by Mechanical Activation. *Bioresour. Technol.* **2011**, *102*, 7953−7958.

(33) Zhang, Y.; Li, W.; Huang, M.; Xu, X.; Jiang, M.; Hu, H.; Huang, Z.; Liang, J.; Qin, Y. Non-Digesting Strategy for Efficient Bioconversion of Cassava to Bioethanol via Mechanical Activation and Metal Salts Pretreatment. *Renewable Energy* **2021**, *169*, 95−103.

(34) Gavilán, H.; Posth, O.; Bogart, L. K.; Steinhoff, U.; Gutiérrez, L.; Morales, M. P. How Shape and Internal Structure Affect the Magnetic Properties of Anisometric Magnetite Nanoparticles. *Acta Mater.* **2017**, *125*, 416−424.

(35) Niu, H.; Wang, Y.; Zhang, X.; Meng, Z.; Cai, Y. Easy Synthesis of Surface-Tunable Carbon-Encapsulated Magnetic Nanoparticles: Adsorbents for Selective Isolation and Preconcentration of Organic Pollutants. *ACS Appl. Mater. Interfaces* **2012**, *4*, 286−295.

(36) Wang, Z.; Ren, R.; Song, H.; Jia, X. Improved Tribological Properties of the Synthesized Copper/Carbon Nanotube Nanocomposites for Rapeseed Oil-Based Additives. *Appl. Surf. Sci.* **2018**, *428*, 630−639.

(37) Liu, H.; Tian, K.; Ning, J.; Zhong, Y.; Zhang, Z.; Hu, Y. One-Step Solvothermal Formation of Pt Nanoparticles Decorated Pt^{2+}-Doped α-Fe_2O_3 Nanoplates with Enhanced Photocatalytic O_2 Evolution. *ACS Catal.* **2019**, *9*, 1211−1219.

(38) Zhang, H.; Wang, L.; Guo, C.; Ning, J.; Zhong, Y.; Hu, Y. Enhanced Photoactivity and Photographstability for Visible-Light-Driven Water Oxidation over $BiFeO_3$ Porous Nanotubes by Modification of Mo Doping and Carbon Nanocoating. *ChemNanoMat* **2020**, *6*, 1325−1331.

(39) Mahmoud, A. E. D.; Stolle, A.; Stelter, M. Sustainable Synthesis of High-Surface-Area Graphite Oxide via Dry Ball Milling. *ACS Sustainable Chem. Eng.* **2018**, *6*, 6358−6369.

(40) Zhang, R. H.; Chen, Q.; He, Z. Y.; Xiong, L. P. In Situ Friction-Induced Amorphous Carbon or Graphene at Sliding Interfaces: Effect of Loads. *Appl. Surf. Sci.* **2020**, *534*, 146990.

(41) Meng, Y.; Su, F.; Chen, Y. Au/Graphene Oxide Nanocomposite Synthesized in Supercritical CO_2 Fluid as Energy Efficient Lubricant Additive. *ACS Appl. Mater. Interfaces* **2017**, *9*, 39549−39559.